

Quantum nondemolition measurement of optical field fluctuations by optomechanical interaction

A. Pontin,^{1,2} M. Bonaldi,^{3,4} A. Borrielli,^{3,4} L. Marconi,⁵ F. Marino,^{2,5} G.
Pandraud,⁶ G. A. Prodi,^{4,7} P.M. Sarro,⁶ E. Serra,^{4,6} and F. Marin^{1,8,5,9,*}

¹*Dipartimento di Fisica e Astronomia, Università di Firenze,
Via Sansone 1, I-50019 Sesto Fiorentino (FI), Italy*

²*Istituto Nazionale di Fisica Nucleare (INFN), Sezione di Firenze,
Via Sansone 1, I-50019 Sesto Fiorentino (FI), Italy*

³*Institute of Materials for Electronics and Magnetism,
Nanoscience-Trento-FBK Division, 38123 Povo, Trento, Italy*

⁴*INFN, Trento Institute for Fundamental Physics and Application, I-38123 Povo, Trento, Italy*

⁵*CNR-INO, L.go Enrico Fermi 6, I-50125 Firenze, Italy*

⁶*Delft University of Technology, Else Kooi Laboratory, 2628 Delft, The Netherlands*

⁷*Dipartimento di Fisica, Università di Trento, I-38123 Povo, Trento, Italy*

⁸*INFN, Sezione di Firenze, Via Sansone 1, I-50019 Sesto Fiorentino (FI), Italy*

⁹*European Laboratory for Non-Linear Spectroscopy (LENS),
Via Carrara 1, I-50019 Sesto Fiorentino (FI), Italy*

Abstract

According to quantum mechanics, if we keep observing a continuous variable we generally disturb its evolution. For a class of observables, however, it is possible to implement a so-called quantum nondemolition measurement: by confining the perturbation to the conjugate variable, the observable is estimated with arbitrary accuracy, or prepared in a well-known state. For instance, when the light bounces on a movable mirror, its intensity is not perturbed (the effect is just seen on the phase of the radiation), but the radiation pressure allows to trace back its fluctuations by observing the mirror motion. In this work, we implement a cavity opto-mechanical experiment based on an oscillating micro-mirror, and we measure correlations between the output light intensity fluctuations and the mirror motion. We demonstrate that the uncertainty of the former is reduced below the shot-noise level determined by the corpuscular nature of light.

Quantum mechanics prescribes that, as soon as we observe a system, we actually perturb it. For a class of observables, however, it is possible to confine the disturbance produced by the measurement to the respective conjugate variables. One can thus implement a so-called Quantum Non-Demolition (QND) measurement [1–4], that allows to keep observing a variable with arbitrary accuracy, or prepare it in a well-known state. For instance, when the light bounces on a movable mirror, its intensity is not perturbed (the interaction just affects the phase of the electromagnetic field), but the radiation pressure allows to trace back the light fluctuations by observing the mirror motion [5]. Here we demonstrate such a QND measurement in a cavity optomechanical experiment based on an oscillating micro-mirror. By measuring the correlation between intensity fluctuations of the output light and the mirror motion, we demonstrate that the uncertainty of the former is indeed reduced below the shot noise level determined by the corpuscular nature of light. This observation represents a key experimental step in the study of quantum interactions between light and macroscopic systems, as well as in mastering quantum measurements. While in a standard partial detection, the photon noise of the remaining, usable light remains inaccessible, a QND measurement allows to implement a quantum noise eater, and can significantly be exploited in high sensitivity, sub-quantum limited instruments. Quantum properties of intense light are carried by the fluctuations of the electromagnetic field quadratures, that are defined from the bosonic operators, after separation of their average coherent amplitude ($a = \langle a \rangle + \delta a$), as $\delta X = \delta a + \delta a^\dagger$ (amplitude quadrature), $\delta Y = -i(\delta a - \delta a^\dagger)$ (phase quadrature) and $\delta X_\phi = \delta X \cos \phi + \delta Y \sin \phi$ (generic quadrature). The possibility to perform a QND measurement of a field quadrature (in particular, of the amplitude δX) by exploiting the radiation pressure exerted on a movable mirror was studied by Jacobs et al. in 1994 [5]. A resonant optical cavity amplifies the intensity fluctuations, and actually the momentum transferred to the mirror by the bouncing photons. The consequent mirror displacement is then enhanced around a mechanical resonance. As suggested later, the measurement of the mirror

motion can be performed interferometrically by a meter field [6, 7].

An ideal QND measurement is defined by a perfect correlation between the variable to be estimated (signal variable) X_s , and the directly measured meter variable Y_m , i.e., by $C_{X_s Y_m} := |S_{X_s Y_m}|^2 / (S_{X_s X_s} S_{Y_m Y_m}) = 1$ where S_{XY} is the cross-correlation spectrum between X and Y , and C_{XY} is the magnitude-squared coherence (MSC). In the optomechanical scheme described above, its achievement is prevented by thermal fluctuations of the movable mirror and by the imprecision of the measurement. More importantly, in a realistic experiment an even weak detuning between input field frequency and cavity resonance, and/or some classical input noise, can create a strong classical correlation between the signal field quadrature X_s , and the meter field Y_m [8]. Therefore, even a $C_{X_s Y_m}$ close to unity is not sufficient to guarantee a QND measurement [9], that can just be achieved if $S_{\Delta X} := S_{X_s X_s} - |S_{X_s Y_m}|^2 / S_{Y_m Y_m} < 1$, i.e., if the information carried by Y_m is sufficient to reduce the residual uncertainty of X_s below the standard quantum fluctuations (shot noise).

Recent advances in cavity optomechanics [10] have allowed to discern the quantum component in radiation pressure [11–13], and in the correlation between signal and meter [12] or between field quadratures after optomechanical interaction [14]. The latter is actually the basic ingredient of the recently observed ponderomotive squeezing [15–17]. These results represent crucial achievements in the study of quantum optomechanical coupling, however no experiment could extract from the mirror motion enough information to prepare a state with residual fluctuations below the shot noise. This is in fact what we are showing in this work, where we actually achieve a measurement of the light quantum noise by observing the effect of the photons impact on a movable mirror.

We have made a moving mirror by coating a silicon micro-oscillator with a high reflectivity multilayer disk (Fig. 1a). The shape of the device is designed to minimize its coupling to the frame and maximize its mechanical quality factor [18, 19] (see Supplemental Material).

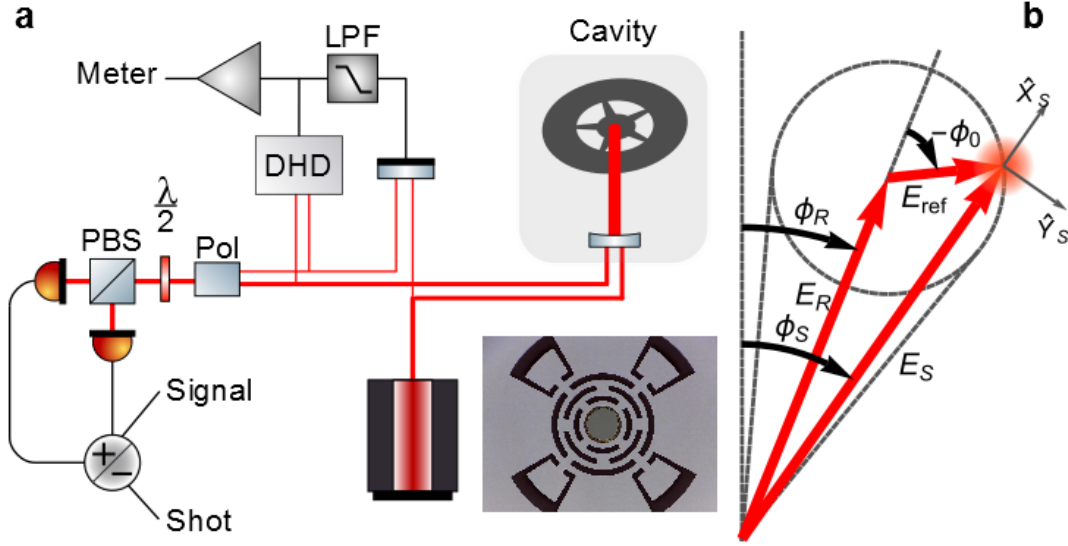


FIG. 1: a) Simplified experimental setup. DHD: double homodyne detection, LPF: low-pass filter, Pol: polarizer. An half-wave plate and a polarizing beam-splitter (PBS) allow a precise 50% splitting. The inset shows an image of the oscillator with the central, 0.4 mm diameter mirror. b) Schematic composition of the fields after the polarizer, in the complex phase plane. The mean field E_S is formed by superposition of the field reflected by the cavity (E_R) and a fraction of the reference field (E_{ref}). By changing the length of the reference arm we can decide the reference phase ϕ_0 and actually the output field phase ϕ_s . The final amplitude quadrature X_s corresponds to the quadrature $X_{(\phi_s - \phi_R)}$ in the reflected field.

It acts as back mirror in a cooled optical cavity, with half linewidth $\kappa/2\pi = 2.85$ MHz. The resonance frequency of the mechanical mode exploited in this work is 169334 Hz, its quality factor 1.1×10^6 . The radiation generated by a Nd:YAG laser is amplitude stabilized, and split into two orthogonally polarized beams, forming the arms of a Michelson interferometer. The strongest beam (the signal) is mode-matched to the optical cavity, with an input power of 38 mW. The length of the second arm (the reference) can be tuned with a controllable mirror. At the output of the interferometer, a wedge window picks up a fraction of the superimposed beams, and sends it to a double homodyne detection (see Supplemental Material), exploiting different

combinations of the two fields and having two purposes. Firstly, it provides a measurement of the phase quadrature of the field reflected by the cavity (we call Y_m the measured fluctuations), that plays the role of the meter. Secondly, its signal is used in a servo loop to stabilize the length of the reference arm and thus fix the reference phase at a desired value. Finally a polarizer, set at a small angle with respect to the signal polarization axis, combines most of the signal field with a small fraction of the reference.

The radiation transmitted by the polarizer is actually the observed physical system, and in particular its amplitude fluctuations are the signal variable X_s . In order to verify that the meter provides a QND measurement of such fluctuations, they are monitored (destructively) with a standard balanced detection, composed of a 50% beam-splitter and a couple of photodiodes: the sum of their signals gives X_s , their difference provides an accurate calibration of the standard quantum level (SQL). Thanks to the weak leakage of the reference field through the polarizer, the phase of the output field is rotated with respect to the radiation reflected by the cavity, by a quantity that can be accurately chosen (see Fig. 1b).

An auxiliary beam, frequency shifted and orthogonally polarized with respect to the signal, is actively locked to a cavity resonance, allowing to precisely set and stabilize a small but non-null detuning between the main beam and the cavity.

The spectrum of the meter (Fig. 2a) is dominated by the fluctuations of the cavity length, mainly due to the oscillating mirror. Therefore, the meter provides indeed a readout for the movable mirror, that in turn performs a measurement of a particular field quadrature (namely, the quadrature that gives rise to the intracavity intensity fluctuations). The optomechanical interaction shifts the frequency of the main oscillator mode to ~ 167500 Hz and broadens its resonance to 430 Hz (corresponding to an effective temperature of ~ 2 mK) [10]. The peak emerges from a background of few 10^{-36} m²/Hz given by the tails of low frequency mechanical modes and of a second oscillator mode at ~ 208 kHz. The laser frequency noise is negligi-

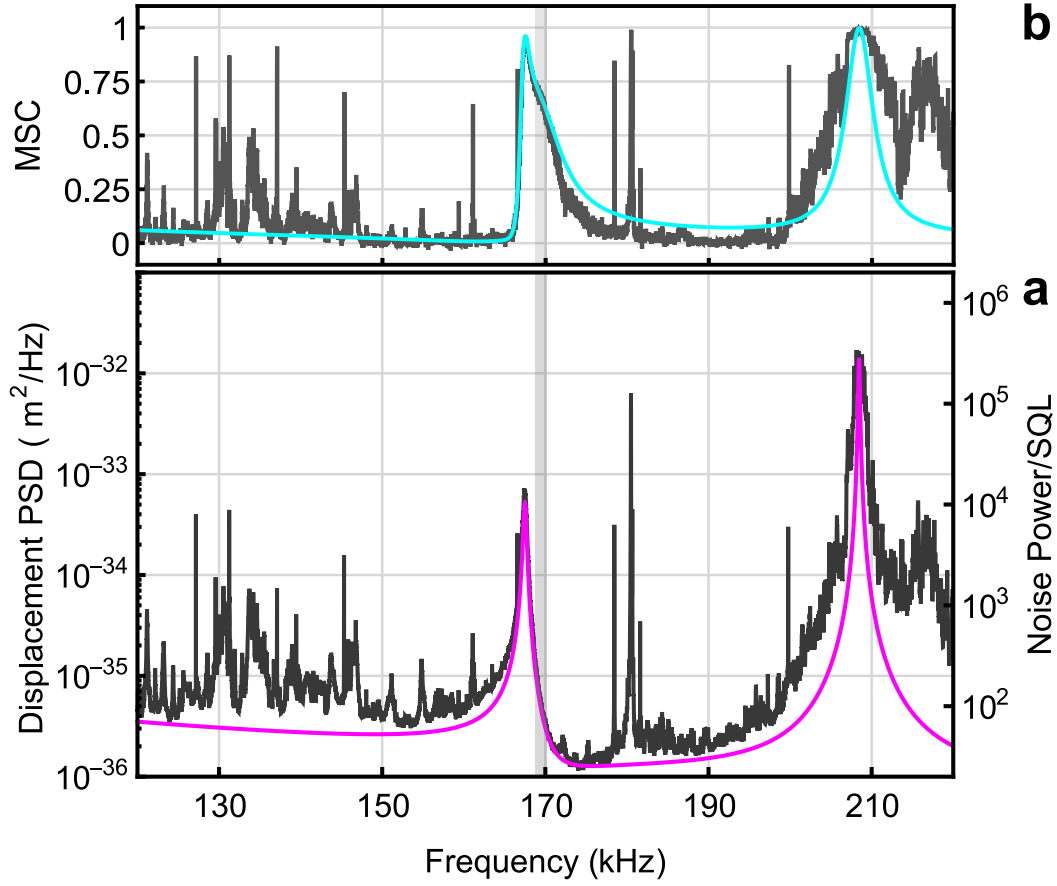


FIG. 2: a) Spectral density of the meter field (black). The spectrum is calibrated both in terms of meter standard quantum noise (right axis), and in terms of single-sided power spectral density (PSD) of cavity displacement noise (left axis). The electronic noise (already subtracted from the displayed spectrum) is 10 dB below the SQL. In the model (magenta) we have introduced phenomenologically a $1/\omega^2$ contribution to account for the tails of low frequency modes, and an additional resonance at ~ 208 kHz. b) Experimental magnitude-squared coherence $C_{X_s Y_m}$ between the output signal and the meter (black), and its theoretical model (cyan). The corresponding signal spectrum is shown in Fig. 3. A shadow shows the frequency region where the QND measurement is realized.

ble. Thermal noise, laser amplitude noise (of classical and quantum origin), and intracavity intensity fluctuations due to the background displacement noise, all contribute with comparable importance to the force noise acting on the oscillator (see Supplemental Material). The last contribution is responsible for the deviation from a Lorentzian shape of the peak, that assumes a Fano profile.

The coherence between the meter and the signal (Fig. 2b) assumes values close to unit around the peak frequency, but it is mainly due to classical fluctuations. Only the following comparison with the signal spectrum allows to assess that a QND measurement is indeed performed.

The spectrum of X_s is shown in Fig. 3 for a particular reference phase. It displays a typical Fano profile, due to the interference between amplitude fluctuations of the intracavity field, which act on the mirror via radiation pressure, and the field fluctuations induced by the consequent mirror motion. For the chosen reference phase, such interference is constructive on the right of the resonance, and destructive on the left, due to the change in the sign of the real part of the mechanical susceptibility [20]. As a consequence, depending on the frequency, the spectral density is higher or lower than the input amplitude power spectrum, but always above the SQL. This behavior is indeed predicted by the theory, and typically occurs for most of the values of the reference phase.

If, on the other hand, we exploit the information carried by the meter and calculate the spectral density $S_{\Delta X}$ of the residual fluctuations, we see that it falls below the shot noise level in a ~ 1.5 kHz broad region, on the high frequency side of the resonance. Its lowest value, normalized to the SQL, is 0.921 ± 0.012 (uncertainty corresponding to one standard error) when the spectrum is integrated over 150 Hz (Fig. 3b). By averaging over a 600 Hz band we obtain 0.942 ± 0.006 , demonstrating a QND measurement with strong statistical significance. The systematic error due to calibration uncertainties is ± 0.005 . To fully exploit the information

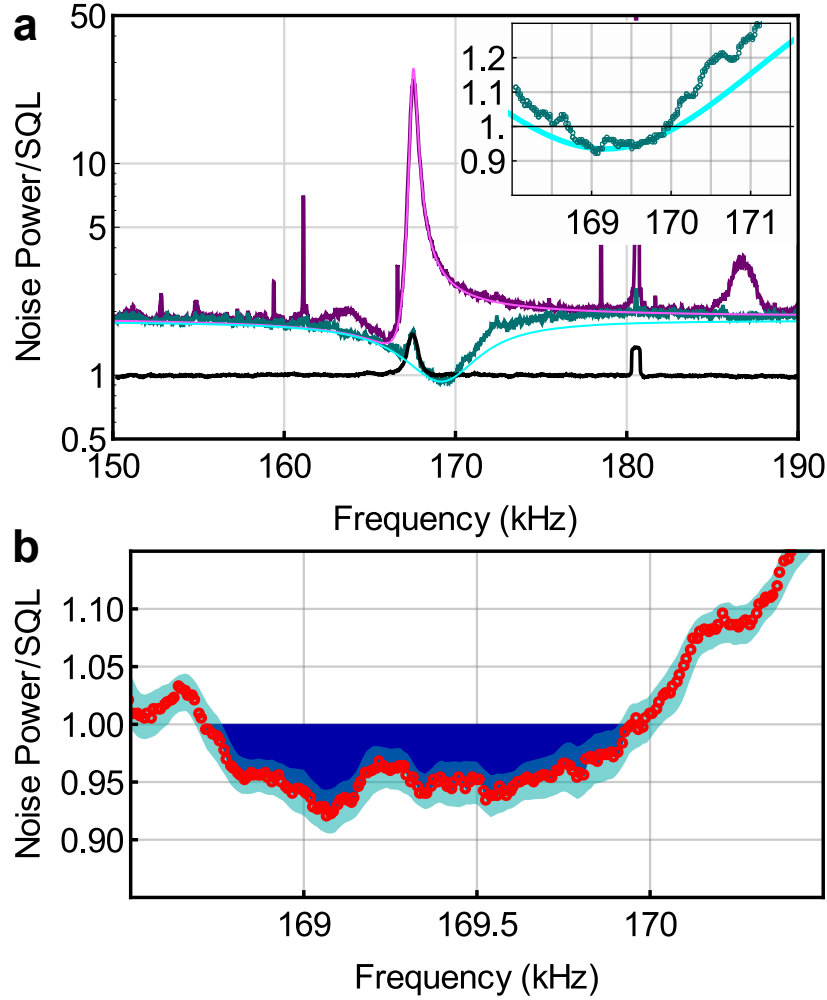


FIG. 3: a) Spectral density of the signal field $S_{X_s X_s}$, normalized to the SQL (wine). From the comparison with the model (magenta) we derive a detuning of -0.016κ and a signal phase $\phi_s = -24$ mrad. Spectral density of the residual fluctuations $S_{\Delta X}$ (dark green), with their model (cyan). Spectrum of the difference between the signals of the photodiodes in the balanced detection, from which the SQL is deduced (black). The electronic noise (already subtracted from the displayed spectra) is 15 dB below the SQL, for both the sum and the difference signals of the balanced detection. The inset shows an enlarged view. b) For $S_{\Delta X}$ we show the result of a flat moving average over a frequency interval of 150 Hz (average value with red symbols, and 90% confidence belt in light blue). The minimum is 0.921 ± 0.012 (uncertainty corresponding to one standard error). By averaging over a 600 Hz band we obtain 0.942 ± 0.006 .

carried by the meter, we have not just used the correlation between X_s and Y_m , but also the one between X_s and the square of Y_m (see Supplemental Material).

We have fitted to the spectrum a complete optomechanical model (see Supplementary Information) where all the system parameters are independently measured, except for the amplitude of the background displacement noise, the detuning and the reference phase. The fact that $S_{\Delta X}$ is below the SQL on just the right hand side of the peak, predicted by the model but not straightforward in a simplified view, is due to the frequency/background noise cancellation occurring around the resonance frequency of the free oscillator [21].

If the reference phase is changed to the opposite side with respect to the reflected field, the destructive interference in X_s occurs on the right of the resonance. By accurately tuning the phase, we can now observe an intensity spectrum $S_{X_s X_s}$ falling below the shot noise level (Fig. 4). It is the signature of ponderomotive squeezing [15–17, 22, 23]. However, the QND measurement is more efficient than the direct squeezing scheme, as it strongly broadens the spectral region where the fluctuations are smaller than the SQL. Moreover, the results are weakly phase-dependent, as indicated by the fact that the sub-SQL region is now very similar to the one obtained with the previous phase value. A QND measurement for state preparation gives similar results to a squeezing experiment with the addition of a frequency-dependent, optimal quadrature rotation [24], and, in principle, it even surpasses its performance.

In a measurement process, the SQL is a crucial threshold: one can reduce the noise down to the SQL by just using, in a noise eater, a beam sampler to measure the intensity fluctuations. On the contrary, a noise level below the shot can just be obtained inside the close loop containing the detector, i.e., in a destructive measurement. In other words, the quantum photon noise remains elusive in classical experiments, and it can just be catch by a QND measurement [9]. This technique is therefore very promising for the application to sub-SQL sensors, including integrated micro-devices and future gravitational wave detectors, where it can either be used

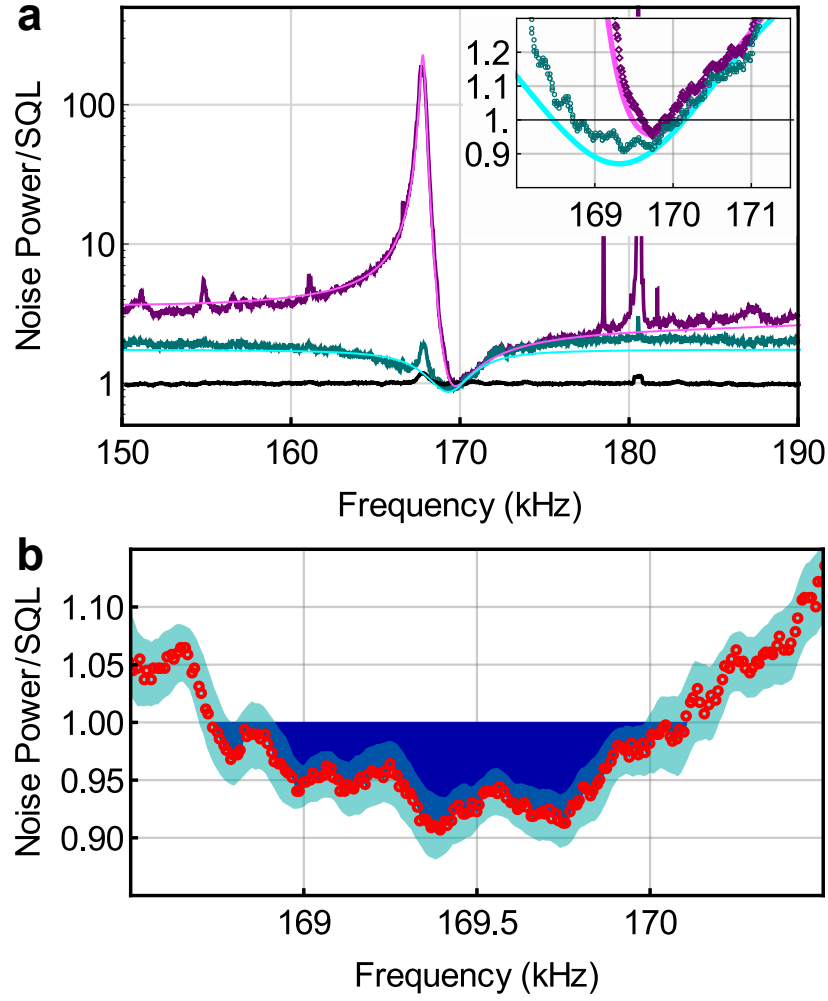


FIG. 4: As in Fig. 3, for a different value of the signal phase (-41.5 mrad) and a slightly different detuning (-0.019κ). The minimal value of the residual fluctuations is 0.906 ± 0.016 when integrated over 150 Hz, and 0.924 ± 0.007 integrating over 600 Hz.

to produce sub-shot noise light in a quantum noise eater, or directly integrated in the complete measurement procedure.

Acknowledgments

This work has been supported by MIUR (PRIN 2010-2011 and QUANTOM) and by INFN (HUMOR project). A.B. acknowledges support from the MIUR under the FIRB Futuro in ricerca 2013 funding program, project code RBFR13QUVI.

Supplemental Material

The optomechanical system

We have fabricated our moving mirror by micro-lithography on a silicon-on-insulator wafer. A detailed description of the fabrication process is reported in Ref. [25], while the design of the device is discussed in Refs. [18, 19]. The oscillator has a particular shape, studied to maximize its mechanical quality factor and isolation from the frame (Fig. 5a). A structure made of alternating torsional and flexural springs supports the central mirror and allows its vertical displacement with a minimal internal deformation, reducing the mechanical loss in the highly dissipative optical coating. For the oscillation mode exploited for this work, the movement of the central disk is balanced by four counterweights, so that the four joints are nodal points (Fig. 5b). Its effective mass is $m = 2.5 \times 10^{-7}$ kg, deduced from the thermal peak in the displacement spectrum measured at room temperature with a Michelson interferometer, its frequency at cryogenic temperature is $\omega_m/2\pi = 169334$ Hz. The quality factor of 1.1×10^6 at cryogenic temperature is measured from the ring-down after excitation, using a Michelson interferometer. In a second oscillation mode, with resonance frequency around ~ 210 kHz, the counterweights move in phase with the central disk (Fig. 5c), therefore a net recoil force is applied on the joints, inducing a larger coupling with the frame and actually a lower quality factor. The design includes an external wheel, working as mechanical filtering oscillator (Fig.

5d), with a resonance frequency of ~ 22 kHz.

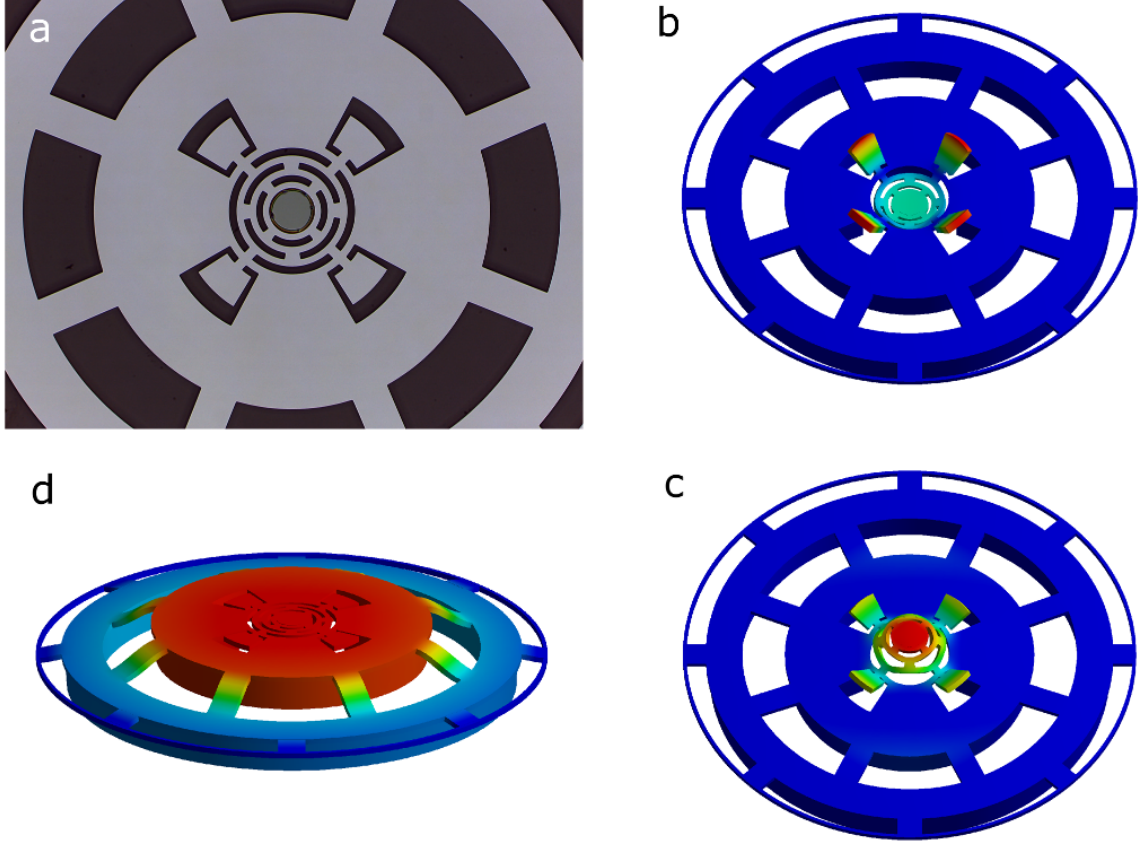


FIG. 5: a) SEM image of the full device, including the central oscillator and the external isolating wheel. The central dark disk is the $400\mu\text{m}$ diameter coating. b-d) FEM simulations of the displacement corresponding to the balanced oscillator mode exploited in this work (b), the second, unbalanced mode (c), and the first wheel oscillator mode (d).

The central coated region of the oscillator is the back mirror of a Fabry-Pérot cavity where the input coupler is a 50 mm radius concave mirror, glued on a piezoelectric transducer used to keep a cavity resonance within the laser tuning range. The cavity length ($L_c = 1.455$ mm) is deduced from the free-spectral-range measured with a tunable laser and a wavemeter. The linewidth (half-linewidth $\kappa/2\pi = 2.85$ MHz) is measured (at cryogenic temperature) by scan-

ning the cavity length over the resonance at low input power, calibrating the scan with phase modulation sidebands at 13.3 MHz. From the calculated Finesse (18055), the measured resonance depth in the reflected intensity, and the measured mode matching of 90%, we deduce an input coupler transmission of 315 ppm (in agreement with the direct measurement, input rate $\kappa_1/2\pi = 2.58$ MHz) and additional cavity losses of 33 ppm (loss rate $\kappa_2/2\pi = 0.27$ MHz). The cavity is strongly overcoupled to optimize the quantum efficiency.

The cavity is mounted and pre-aligned on clean environment, then suspended inside an helium flux cryostat. The first stage of the suspension is formed by a mass-spring system, the second stage is a pendulum. The cavity is thermalized to the cold finger with soft copper foils. The temperature reached by the cavity mount, measured with a diode sensor, is 4.9 K. A finite elements simulation of the heat propagation inside the mount and the silicon device, at the maximum input laser power, suggests that the oscillator temperature should be few tenths of degree higher. The temperature that gives the best agreement between the experimental spectra and the model is indeed 5.6 K.

In Figure 6 we show a spectrum of the cavity phase noise, acquired at cryogenic temperature and calibrated in terms of cavity length changes. A portion of this spectrum is also shown in Figure 2a. The peaks corresponding to the two oscillator modes described above are visible around 168 kHz and 210 kHz. The latter is structured due to the larger coupling with the substrate modes. The peak around 22 kHz is due to the isolating wheel oscillator. Lower frequency peaks are mostly due to the piezoelectric and input mirror modes. Below ~ 20 kHz, the measured spectrum is lower than the real displacement spectrum due to the servo loop of the laser locking.

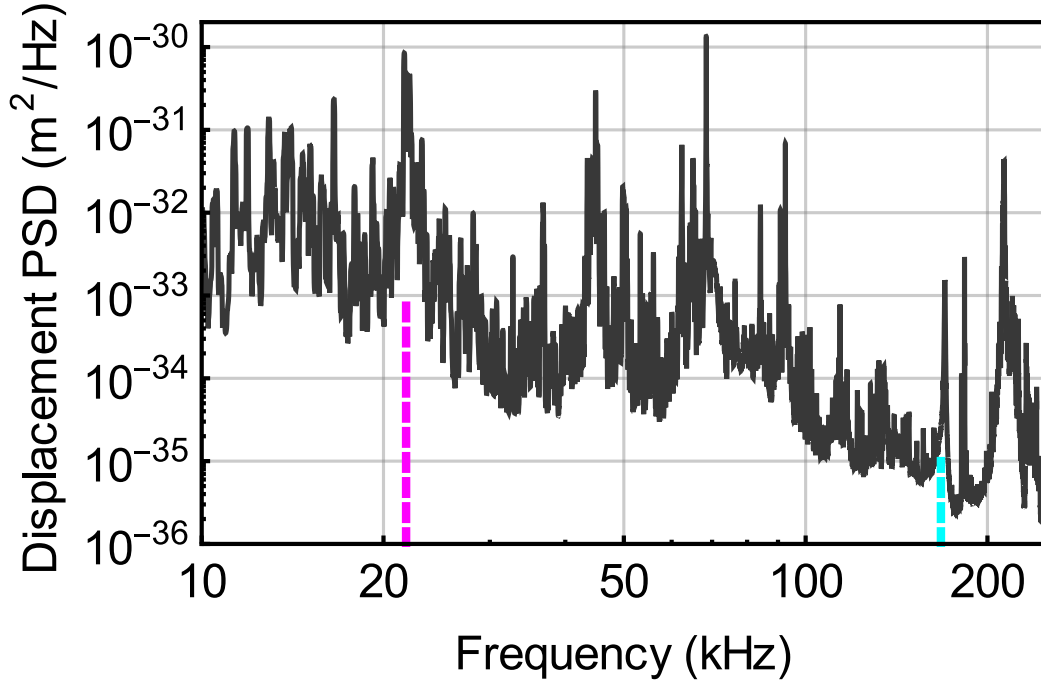


FIG. 6: Phase noise spectrum of the cavity, calibrated as displacement power spectral density (PSD). The magenta and cyan dashed lines indicate respectively the peaks corresponding to the wheel oscillator and the first oscillator mode.

The experimental setup

The experimental setup is sketched in Figure 7. The light source is a cw Nd:YAG laser operating at 1064 nm. On the laser bench, the radiation is split into two beams. The first one (auxiliary beam) is frequency shifted by means of two acousto-optic modulators (AOM) operating on opposite diffraction orders. A resonant electro-optic modulator (EOM) provides phase modulation at 13.3 MHz used for a Pound-Drever-Hall (PDH) detection scheme. The locking bandwidth is about 20 kHz and additional notch filters assure that the servo loop do not influence the system dynamics in the frequency region around the oscillator frequency.

The main beam, with a higher power, is amplitude stabilized with a system composed of an

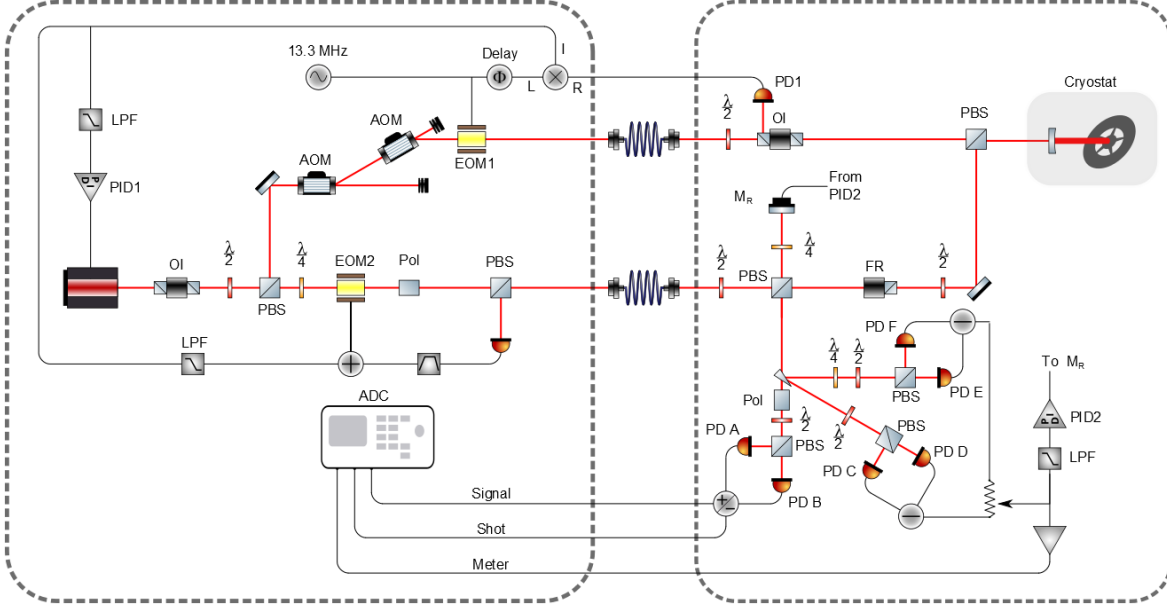


FIG. 7: Detailed scheme of the experimental setup. EOM: electro-optic modulator. AOM: acousto-optic modulator. Pol: polarizer. PBS: polarizing beam-splitter. LPF: low-pass filter. OI: optical isolator. PD: photodiode. FR: Faraday rotator.

electro-optic polarization modulator, a polarizer, a beam-splitter sending a fraction of the laser radiation on a sensing photodiode, whose signal is bandpass filtered between 100 and 200 kHz and fed to the modulator. Our commercial laser is equipped with its internal noise-eater that depresses the relaxation oscillations peak and reduces the relative intensity noise to -140 dB/Hz, corresponding to an amplitude noise (normalized to SQL) of $1 + P/(30\mu\text{W})$, where P is the laser power. After our external stabilizer, noise reduces by about 30 dB, down to $1 + P/(24\text{ mW})$.

The PDH signal, having a linear dependence on the detuning around resonance, is also band-pass filtered around 22 kHz, and added to the signal driving the polarization modulator. We thus implement a feedback cooling [26] on the wheel oscillator, with two purposes: firstly, we improve its dynamic stability, that is otherwise critical due to the combined effect of optomechan-

ical interaction and frequency locking servo loop [27]. Secondly, we depress the fluctuations of the wheel oscillator, that would otherwise provide a major contribution to the overall cavity phase noise. We remark that the rms value of such phase noise is large enough that a simple linear expansion of the cavity optical response is not sufficient to account for the reflected field fluctuations. Therefore, even if feedback cooling is just effective on the peak of the wheel resonator, it reduces the contribution brought into the frequency range of interest by nonlinear mixing.

Both beams are sent to the experiment bench by means of single-mode, polarization maintaining optical fibers. The main beam is split by a polarizing beam-splitter (PBS) and sent into the two arms of a Michelson interferometer. At the end of the reference arm, the beam is focused on a mirror, the position of which is finely controlled with an inductive transducer. On the other arm, the beam is overlapped to the auxiliary beam, with orthogonal polarizations, in a further PBS and then mode-matched to the optical cavity. The laser power impinging on the cavity is about $50\mu\text{W}$ from the auxiliary beam, and 38 mW from the main beam. The calculated intracavity power is 350 W , corresponding to $n_c = 1.8 \times 10^{10}$ photons.

The reflected auxiliary beam, on its back path, is deviated by the input polarizer of an optic isolator and collected by a photodiode for the PDH detection and laser frequency locking. Two optical circulators are also present on the path of the main beam, namely a quarter-wave plate on the reference arm, and a Faraday rotator plus an half-wave plate on the cavity arm, before the second PBS. As a consequence, the beams reflected along both arms are sent to the output port of the Michelson interferometer, where they are overlapped with orthogonal polarizations.

On the path of the beam exiting from the Michelson interferometer, the two faces of a wedge window, with the bisector plane at the Brewster angle, pick up 1.5% each of the p-polarized light arriving from the cavity, and respectively 6% and 23% of the s-polarized light from the reference beam. On the path of one of these reflections, a quarter-wave plate with the axis parallel to

the polarizations adds an additional delay between the fields arriving from the cavity and the reference arms. Both beams are analyzed by homodyne setups, each composed of an half-wave plate that rotate the polarizations by 45° , a PBS, and a couple of photodiodes at the two outputs of the PBS. The difference signals of the two couples of photodiodes can be written respectively as $V_A \sin \phi$ and $V_B \cos \phi$, where ϕ is the phase difference between the fields coming from the two arms of the Michelson interferometer. The transimpedance gains of the two couples of photodiodes are set to compensate for the different collected powers, in order to have $V_A \simeq V_B$. We derive a weighted average of the two signals $V_m = \beta V_A \pm (1-\beta) V_B \propto \sin(\phi + \phi_0(\beta))$, where β can be chosen between 0 and 1 and thus $-\pi/2 < \phi_0 < \pi/2$. The low frequency component of V_m is integrated and fed back to the position control of the reference arm mirror, so that the phase ϕ is locked to $-\phi_0$ with a servo bandwidth of about 1 kHz. Moreover, the fluctuations of δV_m are now proportional to the fluctuations of the phase quadrature of the field reflected by the cavity, plus a contribution that, due to the low detected power, can be considered as originated by additional vacuum fluctuations. In summary, such combined homodyne detection is equivalent to a standard homodyne detection of the phase quadrature of the cavity reflected field, and it additionally allows to choose and stabilize the phase difference between the two, orthogonally polarized fields that compose the main beam going to the subsequent detection. We identify δV_m with our meter Y_m .

After the wedge window, the main beam is filtered by an high extinction polarizer. The axis of the transmitted polarization is very close to the p-polarization axis (within $\sim 1^\circ$), so that $> 99\%$ of the field from the cavity and $\sim 3\%$ of the field from the reference arm (corresponding to about $2\mu\text{W}$) are transmitted and superimposed to form the signal field. The ratio between the laser powers coming from the two arms is here $\sim 10^{-4}$, allowing to tune the signal phase, with respect to the field reflected by the cavity, by about $\pm 10^{-2}$ rad (Fig. 1b).

At the end, the signal is analyzed by a balanced detection. The signals from the two photo-

diodes are high-pass filtered, amplified, and combined to obtain their sum and difference, that are filtered with high order low-pass, anti-aliasing circuits and acquired by an high resolution digital scope. We remark that a very well defined linear polarization, guaranteed by the high extinction polarizer, is crucial for the correct working of the subsequent balanced detection, in particular for reliably using the difference between the photodiodes signals as a measurement of the SQL.

Data acquisition and calibrations

The balanced detection is optimized by minimizing, in the difference signal, the residual of an amplitude modulation peak at ~ 170 kHz, introduced just for this setting on the modulator of the noise-eater, with the laser frequency far from cavity resonance. The measured rejection is ~ 40 dB. The total quantum efficiency in the detection of the field reflected by the cavity is 69%, including the losses in the wedge window and in the polarizer, and the $\sim 90\%$ efficiency of the homodyne photodetectors.

The low-pass filters of the sum and difference signals are calibrated by measuring their (nominally equal) transfer functions, with a relative accuracy of better than 0.1%. We have also calibrated the scope channels used for the sum and difference signals, at all the vertical scales used in the experiment. The corrections applied arrive to 2%. We have finally checked the overall calibration by sending the laser radiation on one single photodetector, and verifying that the corrected sum and difference signals are equal to within 0.1%.

The linearity of the difference signal versus the detected photocurrent (sum of the two detectors photocurrents) has been checked by sending to the photodiodes the laser radiation of the main beam very far from cavity resonance. The result is shown in Figure 8(b-c). The residuals of the linear fit show no systematic deviation. The noise variance reported in the figure is calculated by considering the spectrum of the difference signal in the intervals 154 – 163 kHz and

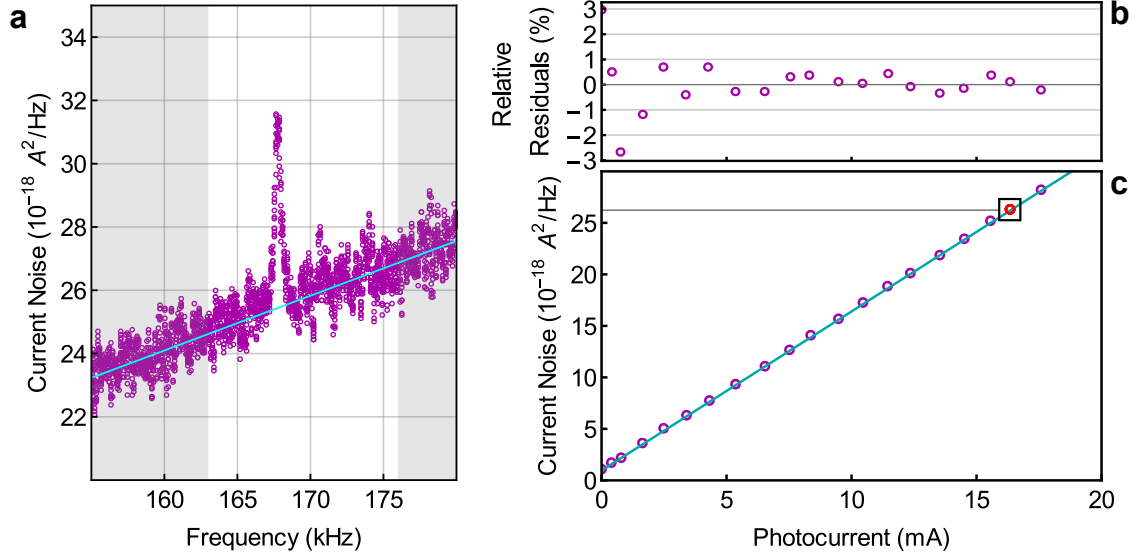


FIG. 8: c) Current noise spectral density at 170 kHz measured in the difference signal of the balanced detection, versus total photocurrent, measured by varying the optical power impinging on the detectors. The cyan straight line is a linear fit to the data. The red circle indicates a typical measurement taken with the fully working experiment, used to calibrate the SQL for the spectra shown in the main article. b) Residuals of the fitting procedure. a) Spectral density of the difference signal, acquired during the experiment. The shadowed region is used for the linear regression shown with a cyan straight line, that is actually used to evaluate the SQL (as well as the spectral density values shown in the panel (c)). The peak at ~ 168 kHz is the remnant of the signal due to the oscillator.

176 – 180 kHz, and calculating the spectral density at 170 kHz with a linear interpolation. Such linear interpolation is sufficient to account for the fact that the spectrum is not white, due to the high-pass filters in the photodetectors circuits. The same procedure is used for evaluating the SQL in the experimental data, where we exclude in this way the region (163 – 176 kHz) where the strong oscillator peak could percolate into the difference signal in spite of the high rejection. The electronic noise is equal to the shot-noise of 0.63 mA, equivalent to an impinging power of 0.8 mW, and it has a day-to-day reproducibility of $\sim 10\%$. Since it is subtracted from the

measured spectra, it contributes to the uncertainty with an additional 0.3%. Taking into account all the analyzed sources of systematic error, we evaluate that their total effect in the calibration of the spectra to the SQL is below 0.5%.

We have acquired simultaneous data streams from three channels: the sum and difference signals from the final balanced detection, and the meter Y_m . The signals are sampled at 5 MHz and several 10 seconds data streams are acquired, separated by lapses of few seconds necessary for data storage. Such delays improve the randomness of the complete data sets, reducing the effect of long term relaxations. The stability of the mean beam power is better than 1% during the whole measurement period. The data elaborated to obtain the results shown in Figures 3 and 4 are taken respectively from 5 and 4 consecutive 10s time series.

Data analysis

The 10 seconds temporal series are divided into 100 ms long intervals. A preliminary selection on the intervals is performed by setting upper limits on the peak and rms values of the sum signal. This selection procedure is useful to reject datasets plagued by strong noise spikes, mainly due to low (\sim kHz) frequency modes, generated by instabilities of the helium flux in the cryostat. We keep $\sim 90\%$ of the data intervals.

For each n -th interval, we calculate the discrete Fourier transform of the difference signal $\tilde{X}_-^{(n)}$, of the sum signal $\tilde{X}_+^{(n)}$, of the meter signal $\tilde{Y}_m^{(n)}$, of the square of the meter signal $\tilde{Y}_{\text{sqm}}^{(n)}$ (we distinguish in the following the experimental signal \tilde{X}_+ from the signal variable X_s that is obtained from \tilde{X}_+ after subtraction of the electronic noise and normalization to the SQL).

The spectra to be evaluated are the sum and difference power spectra $S_{X_+X_+}$ and $S_{X_-X_-}$, and the cross-correlation contributions. For all such spectra, we use correct estimators as discussed below in the sub-section “The statistical estimators”. The final steps of the analysis are the subtraction of the detection electronic noise, and the normalization of the sum and the residual

spectra to the SQL. The obtained $S_{X_s X_s}$ is plotted in Figures 3 and 4 (wine traces).

As already mentioned, due to the relatively large rms value of the cavity phase noise, mainly due to several mechanical resonances, a simple linear expansion of the cavity reflection function is not sufficient to account for the whole effect of such noise on the reflected field quadratures. As a consequence, a non-null correlation also exists between X_+ and the square of Y_m , and a complete measurement of the signal state must be performed by using all the information provided by the meter signal, i.e., both the correlation with Y_m and that with its square. This is accomplished by subtracting from $S_{X_+ X_+}$ also the correlation between X_+ and Y_{sqm} . This is indeed the spectrum of the residual fluctuations that we have plotted in Figures 3 and 4 (dark green traces). It is compared with the theoretical calculation of $S_{\Delta X}$, that is based on linear expansions of the equations of motion, and is produced by the main opto-mechanical interaction. We remark however that even without the use of the correlation with Y_{sqm} , the spectrum of the residual fluctuations falls below the unit. No further improvements have been obtained by considering correlation with higher order in Y_m .

Even the subtraction of just the correlation with Y_{sqm} from the spectrum $S_{X_+ X_+}$ is interesting, as shown in Figure 9, since it removes some peaks originating from the nonlinearity of the system, improving the agreement with the model. We point out that this is a confirmation of the existence of a quadratic nonlinearity. The correlation with Y_{sqm} is particularly meaningful around two peaks at ~ 163 kHz and ~ 187 kHz, but it also slightly improves the residual around the minimum.

The statistical estimators

In this work we have to estimate power spectra (such as $S_{X_+ X_+}$ and $S_{X_- X_-}$), as well as cross-correlation contributions (such as $|S_{X_+ Y_m}|^2 / S_{Y_m Y_m}$), starting from a finite number N of experimental, Fourier transformed time series. For the power spectrum of a variable X , a good

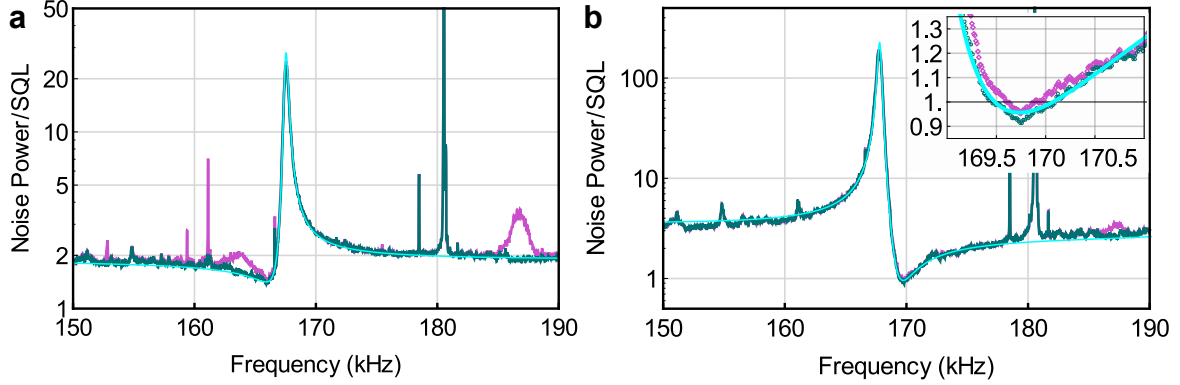


FIG. 9: a) Spectra of the signal (experimental spectrum of the sum signal from the homodyne detection, with the electronic noise subtracted, and normalized to SQL) (purple), of the residual fluctuations after subtraction of the correlation with the square of the meter (dark green), and theoretical model (cyan), for the reference phase corresponding to Figure 3. b) The same, for the reference phase corresponding to Figure 4. The inset displays an enlarged view around the minimum, showing the improvement of the ponderomotive squeezing when the correlation with Y_{sqm} is subtracted from the spectrum.

estimator is straightforwardly $\hat{S}_{XX} = \sum_{n=1,N} |\tilde{X}^{(n)}|^2 / N$. On the other hand, finding a correct, unbiased indicator for the cross-correlation contribution is not obvious. We have therefore chosen a different point of view.

We are willing to estimate the residual fluctuations of X that remains once the information brought by Y is optimally used (the subscripts of X and Y are omitted in this discussion for the sake of clarity). In a linear system, the fluctuation that can be extracted from Y can be written as $\alpha(\omega)\tilde{Y}$, where $\alpha(\omega)$ is a complex function. Therefore, we have to find $\alpha(\omega)$ that minimizes the spectral density of $S_{\Delta X}^\alpha := \langle |\tilde{X} - \alpha\tilde{Y}|^2 \rangle = S_{XX} + |\alpha|^2 S_{YY} - 2\text{Re}(\alpha S_{XY})$. By deriving with respect to α , we find that its optimal value is

$$\alpha_{\text{opt}} = (S_{XY})^* / S_{YY} \quad (1)$$

and the lowest residual spectrum is indeed

$$S_{\Delta X}^{\text{opt}} = S_{XX} - |S_{XY}|^2 / S_{YY} . \quad (2)$$

Any different α gives an overestimation of the optimal residual spectrum. On the other hand, for a given α , we have a correct, unbiased estimator of the residual spectrum, that is

$$\hat{S}_{\Delta X}^{\alpha} = 1/N \left(\sum |\tilde{X}^{(n)}|^2 + |\alpha|^2 \sum |\tilde{Y}^{(n)}|^2 - 2\text{Re} \left(\alpha \sum (\tilde{X}^{(n)})^* \tilde{Y}^{(n)} \right) \right) . \quad (3)$$

The function α could be chosen *a priori*, e.g. on the basis of a model, but for a more realistic analysis we have derived it from the experimental data using the Eq. (1) as guideline. We separate the N intervals into two independent half-sets, according to the parity of the index n . From the first half-set, we calculate α as

$$\alpha_{\text{odd}} = \frac{\sum_{\text{odd } n} \tilde{X}^{(n)} (\tilde{Y}^{(n)})^*}{\sum_{\text{odd } n} |\tilde{Y}^{(n)}|^2} \quad (4)$$

and from the second half-set, we calculate the residual spectrum following Eq. (3), where the sums are taken over the even indexes. We then repeat the procedure by exchanging the two half-sets, and we finally take the average over the two resulting residual spectra. If we calculate the expectation value of our final spectrum $S_{\Delta X}^{\text{exp}}$, we find:

$$\begin{aligned} E[S_{\Delta X}^{\text{exp}}] &= \frac{1}{N} \langle \sum_{\text{even } n} |\tilde{X}^{(n)}|^2 + |\alpha_{\text{odd}}|^2 \sum_{\text{even } n} |\tilde{Y}^{(n)}|^2 - 2\text{Re}(\alpha_{\text{odd}} \sum_{\text{even } n} (\tilde{X}^{(n)})^* \tilde{Y}^{(n)}) \\ &\quad + \text{even} \leftrightarrow \text{odd} \rangle \\ &= S_{XX} + \langle |\alpha_{e/o}|^2 \rangle S_{YY} - 2\text{Re}(\langle \alpha_{e/o} \rangle S_{XY}) \end{aligned}$$

where we have used the independence of the two half-data sets, so that, e.g., $\langle \alpha_{\text{odd}} \sum_{\text{even } n} f^{(n)} \rangle = \langle \alpha_{\text{odd}} \rangle \langle \sum_{\text{even } n} f^{(n)} \rangle$ and $\langle \alpha_{\text{odd}} \rangle = \langle \alpha_{\text{even}} \rangle := \langle \alpha_{e/o} \rangle$. Since $\langle |\alpha_{e/o}|^2 \rangle \geq |\langle \alpha_{e/o} \rangle|^2$ (a relation valid for any stochastic variable $\alpha_{e/o}$), we can write

$$E[S_{\Delta X}^{\text{exp}}] \geq S_{\Delta X}^{\langle \alpha_{e/o} \rangle} \geq S_{\Delta X}^{\text{opt}} . \quad (5)$$

Therefore, our experimental evaluation of the residual spectrum provides an unbiased, conservative estimator of the residual spectrum.

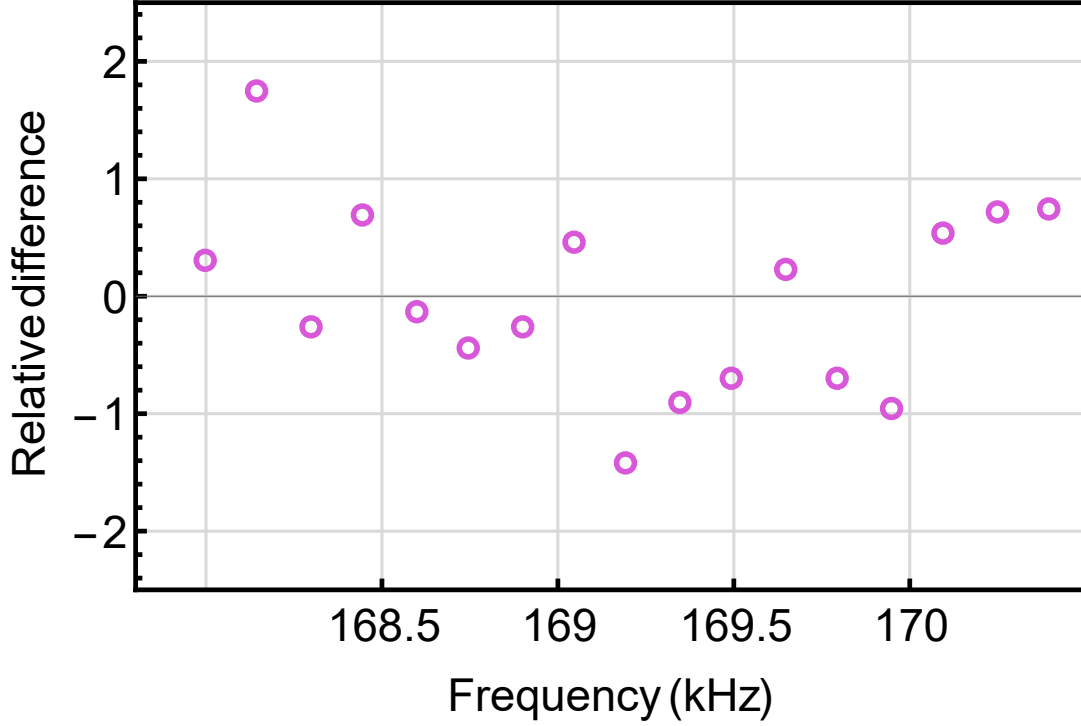


FIG. 10: Difference between the “odd” and “even” estimates of the residual fluctuations, normalized to its statistical uncertainty.

We have tested the compatibility of the two independent “odd”/“even” estimates by calculating their difference normalized to its statistical uncertainty (i.e., to twice the standard deviation of their average). The result is shown in Figure 10 for the QND frequency region of Fig. 4b. The normalized differences have an average value of -0.024 ± 0.21 and a standard deviation of 0.86 ± 0.21 , figures compatible with a normal distribution.

The above discussion can be extended to the case of two information channels Y_1 and Y_2 , as follows. We have to find the functions α_1 and α_2 that minimizes the spectrum of $(X - \alpha_1 Y_1 - \alpha_2 Y_2)$. The residual spectrum is

$$S_{\Delta X} = S_{XX} + |\alpha_1|^2 S_{Y_1 Y_1} + |\alpha_2|^2 S_{Y_2 Y_2} - 2\text{Re}(\alpha_1 S_{X Y_1}) - 2\text{Re}(\alpha_2 S_{X Y_2}) + 2\text{Re}(\alpha_1^* \alpha_2 S_{Y_1 Y_2}) \quad (6)$$

and the optimal weight functions are

$$\alpha_{1,\text{opt}} = \frac{S_{Y_2 Y_2} S_{X Y_1}^* - S_{X Y_2}^* S_{Y_1 Y_2}}{S_{Y_1 Y_1} S_{Y_2 Y_2} - |S_{Y_1 Y_2}|^2} \quad (7)$$

$$\alpha_{2,\text{opt}} = \frac{S_{Y_1 Y_1} S_{X Y_2}^* - S_{X Y_1}^* S_{Y_2 Y_1}}{S_{Y_1 Y_1} S_{Y_2 Y_2} - |S_{Y_1 Y_2}|^2}. \quad (8)$$

As in the case of the single correlation, in order to derive a correct estimator one can separate the data streams into two interlaced subsets, calculate the weight functions from the above expression using, in place of the spectra, averages on half-sets of the correspondent discrete Fourier transforms, calculate the residual spectra $S_{\Delta X}$ according to Eq. (6), exchange the two subsets, and finally average the two results.

In our experiment, we have one single meter Y_m . However, a linear approximation is not sufficient to fully exploit it. The best estimate of X_s would be a function $f(Y_m)$, that we can ideally expand to the second order, as $f(Y_m) \simeq \alpha_1(\omega)Y_m + \alpha_2(\omega)Y_{\text{sqm}}$, thus returning to the previous, two channels case. In the ideal case of an infinite number of measurements in a stationary system, the addition of further orders in Y_m can just improve the estimate. However, in the case of N measurements each further channel adds statistical uncertainty. Moreover, the non-optimal estimator can even increase the residual spectrum if the correlation is not sufficiently strong. As already mentioned, in our case we have indeed verified that the residual spectrum is not further improved by considering higher order terms in Y_m .

The model

The Hamiltonian of the optomechanical system can be written as

$$H = \hbar\omega_c a^\dagger a + \frac{1}{2}\hbar\omega_m(p^2 + q^2) - \hbar G_0 a^\dagger a q \quad (9)$$

where a is the annihilation operator of the cavity mode at frequency ω_c , p and q are the momentum and position operators of the mechanical oscillator, the single-photon coupling strength is

$$G_0 = -(\omega_c/L_c)\sqrt{\hbar/m\omega_m}.$$

The evolution equations for the system are derived from the Hamiltonian with the inclusion of an intense laser field at frequency ω_0 , input vacuum field operators a_1^{in} (from the input mirror) and a_2^{in} (from cavity losses), and additional noise terms that will be listed below. They can be written in the frame rotating at the laser frequency, that is detuned by $\Delta_0 = \omega_0 - \omega_c$ with respect to the cavity resonance, as

$$\dot{q} = \omega_m p, \quad (10)$$

$$\dot{p} = -\omega_m q - \gamma_m p + G_0 a^\dagger a + \xi, \quad (11)$$

$$\begin{aligned} \dot{a} = & -\kappa a + i(\Delta_0 + \zeta + G_0 q) a + E_0 \\ & + \sqrt{2\kappa_1}(a_1^{\text{in}} + \epsilon) + \sqrt{2\kappa_2}a_2^{\text{in}}. \end{aligned} \quad (12)$$

Here $E_0 = \sqrt{2\kappa_1 P/\hbar\omega_0}$ where P is the input laser power and we take E_0 as real, which means that we use the driving laser as phase reference for the optical field. The mechanical mode is affected by a viscous force with damping rate γ_m and by a Brownian stochastic force $\xi(t)$. We have included the laser excess amplitude noise with the real stochastic variable ϵ . The additional cavity phase fluctuations are introduced by a stochastic term ζ in the detuning. The input fields correlations are

$$\langle a_j^{\text{in}}(t)a_j^{\text{in}}(t') \rangle = \langle a_j^{\text{in},\dagger}(t)a_j^{\text{in},\dagger}(t') \rangle = \langle a_j^{\text{in},\dagger}(t)a_j^{\text{in}}(t') \rangle = 0, \quad (13)$$

$$\langle a_j^{\text{in}}(t)a_j^{\text{in},\dagger}(t') \rangle = \delta(t - t'), \quad j = 1, 2. \quad (14)$$

We consider the motion of the system around a steady state characterized by the intracavity electromagnetic field of amplitude α_s , and the oscillator at a new position q_s , by writing:

$$q = q_s + \delta q, \quad (15)$$

$$p = p_s + \delta p, \quad (16)$$

$$a = \alpha_s + \delta a. \quad (17)$$

Substituting Eqs. (15)-(17) into Eqs. (10)-(12), we obtain the stationary solutions:

$$q_s = \frac{G_0}{\omega_m} |\alpha_s|^2, \quad (18)$$

$$p_s = 0, \quad (19)$$

$$\alpha_s = \frac{E_0}{\kappa - i\Delta}, \quad (20)$$

where $\Delta = \Delta_0 + G_0 q_s$, and the first order linearized equations for the fluctuations operators

$$\delta \dot{q} = \omega_m \delta p, \quad (21)$$

$$\delta \dot{p} = -\omega_m \delta q - \gamma_m \delta p + G_0 (\alpha_s \delta a^\dagger + \alpha_s^* \delta a) + \xi, \quad (22)$$

$$\delta \dot{a} = -(\kappa - i\Delta) \delta a + iG_0 \alpha_s \delta q + \sqrt{2\kappa_1} (a_1^{\text{in}} + \epsilon) + i\alpha_s \zeta + \sqrt{2\kappa_2} a_2^{\text{in}}. \quad (23)$$

The Fourier transformed of Eqs. (21)-(23), are solved for $a(\omega)$ (we call $a(\omega)$ the Fourier transformed of $\delta a(t)$ and $a^\dagger(\omega)$ the Fourier transformed of $\delta a^\dagger(t)$, with the same notation for the other fields). Using the input/output relations

$$E_R = \sqrt{2\kappa_1} \alpha_s - \frac{E_0}{\sqrt{2\kappa_1}}, \quad (24)$$

$$a^{\text{out}} = \sqrt{2\kappa_1} \delta a - (a_1^{\text{in}} + \epsilon), \quad (25)$$

we can write the output field, with average value

$$E_R = \sqrt{\frac{P}{\hbar\omega_0}} \frac{\kappa - 2\kappa_2 + i\Delta}{\kappa - i\Delta} \quad (26)$$

and fluctuation operator

$$\begin{aligned} a^{\text{out}}(\omega) = & \nu_1(\omega) a_1^{\text{in}}(\omega) + \nu_2(\omega) a_1^{\text{in},\dagger}(\omega) + \nu_3(\omega) a_2^{\text{in}}(\omega) + \nu_4(\omega) a_2^{\text{in},\dagger}(\omega) \\ & + \nu_5(\omega) \zeta(\omega) + \nu_6(\omega) \epsilon(\omega) + \nu_7(\omega) \xi(\omega), \end{aligned} \quad (27)$$

where

$$\begin{aligned}
\nu_1(\omega) &= \frac{\kappa - 2\kappa_2 + i(\Delta + \omega)}{\kappa - i(\Delta + \omega)} + \frac{i|G|^2\kappa_1\chi_{\text{eff}}(\omega)}{[\kappa - i(\Delta + \omega)]^2}, \\
\nu_2(\omega) &= \frac{iG^2\kappa_1\chi_{\text{eff}}(\omega)}{[\kappa - i(\Delta + \omega)][\kappa + i(\Delta - \omega)]}, \\
\nu_3(\omega) &= \sqrt{\frac{\kappa_2}{\kappa_1}}(\nu_1(\omega) + 1), \\
\nu_4(\omega) &= \sqrt{\frac{\kappa_2}{\kappa_1}}\nu_2(\omega), \\
\nu_5(\omega) &= \frac{i\alpha_s}{\sqrt{2}\kappa_1}(\nu_1(\omega) - \nu_2(\omega) + 1), \\
\nu_6(\omega) &= \nu_1(\omega) + \nu_2(\omega), \\
\nu_7(\omega) &= \frac{iG\sqrt{\kappa_1}\chi_{\text{eff}}(\omega)}{\kappa - i(\Delta + \omega)}.
\end{aligned}$$

Here $G = G_0\sqrt{2}\alpha_s$ is the effective coupling strength, and

$$\chi_{\text{eff}}(\omega) = \omega_m \left[\omega_m^2 - \omega^2 - i\omega\gamma_m + \frac{|G|^2\Delta\omega_m}{(\kappa - i\omega)^2 + \Delta^2} \right]^{-1} \quad (28)$$

is the effective mechanical susceptibility modified by the optomechanical coupling.

In the experiment, we split the output field into a weak meter and a signal. They have different optical losses, that are considered in the model using the beam-splitter relations

$$a_m = \sqrt{\eta_m} a^{\text{out}} + \sqrt{1 - \eta_m} a_3 \quad (29)$$

$$a_s = \sqrt{\eta_s} a^{\text{out}} + \sqrt{1 - \eta_s} a_4 \quad (30)$$

where $a_{3,4}$ are vacuum input fields and $\eta_{m,s}$ are the efficiencies respectively for the meter and the signal. The correlation between a_3 and a_4 could be considered by introducing in the model the beam-splitter that separates the meter and signal fields, followed by further beam-splitters modeling the optical losses. However, due to the low efficiency η_m , to reproduce the results we can safely neglect such correlation and consider vacuum fields $a_{3,4}$ satisfying the relations (13)-(14) with j extended to (3,4). We can similarly consider the reference field as

contributing to the meter and the signal with independent effective vacuum fields, already included phenomenologically in $a_{3,4}$. To account for the non perfect mode matching we must consider that the field in the non-resonant modes is reflected by the cavity input mirror, and impinges on the detectors where, in first approximation, it does not interfere with the main mode. Therefore, we do not sum the fields, but the fluctuating intensities. The above relations are modified by replacing $P \rightarrow \eta_{mm}P$, $(a_1^{\text{in}} + \epsilon) \rightarrow \sqrt{\eta_{mm}}(a_1^{\text{in}} + \epsilon) + \sqrt{1 - \eta_{mm}}a_5$ and $a^{\text{out}} \rightarrow \sqrt{\eta_{mm}}a^{\text{out}} + \sqrt{1 - \eta_{mm}}(\sqrt{1 - \eta_{mm}}(a_1^{\text{in}} + \epsilon) - \sqrt{\eta_{mm}}a_5)$ where η_{mm} is the mode matching coefficient and a_5 is a further vacuum input field.

The general quadrature of a field a is defined as $ae^{-i\phi} + a^\dagger e^{i\phi}$. For the meter field, we measure the phase quadrature with respect to the field reflected by the cavity. The latter, according to Eq. (26), is dephased by $\phi_R = \arctan \Delta/(\kappa - 2\kappa_2) + \arctan \Delta/\kappa$ with respect to our reference (i.e., the field at the cavity input). The measured quadrature of the meter is therefore defined by $\phi_m = \phi_R + \pi/2$. Concerning the signal, we are defining as X_s the amplitude quadrature at the output of the polarizer, i.e., the quadrature defined by the superposition of main and reference fields: $\phi_s = \phi_R - \arcsin \left(\sin \phi_0 / \sqrt{1 + P_R/P_{\text{ref}} + 2\sqrt{P_R/P_{\text{ref}}} \cos \phi_0} \right)$ where P_R (P_{ref}) is the power transmitted by the polarizer and coming from the cavity (reference) arm (Fig. 1b).

Theoretical curves are obtained by calculating symmetrized power spectra and cross-correlation spectra of the variables $Y_m = a_m(\omega)e^{-i\phi_m} + a_m^\dagger(\omega)e^{i\phi_m}$ and $X_s = a_s(\omega)e^{-i\phi_s} + a_s^\dagger(\omega)e^{i\phi_s}$. The oscillator and cavity parameters, quoted above, are all measured independently and fixed in the theoretical calculation. The calculated coupling strengths are $G_0/2\pi = -3.85$ Hz and $G/2\pi = -740$ kHz (at resonance). The input power is $P = 38$ mW. The spectrum $S_{\epsilon\epsilon}$ is 1/4 of the excess intensity noise, normalized to SQL. In our case, we set $S_{\epsilon\epsilon} = 0.25 \times P/(24\text{mW})$. The stochastic term in the detuning is linked to the cavity length fluctuations δl by $\zeta = \delta l \times \omega_c/L_c$. Its spectrum is modeled with a Lorentzian peak at 208 kHz that roughly reproduces the resonance of the second oscillator mode, plus a $1/\omega^2$ background. The

total background amplitude is left as free fitting parameters. The mode-matching parameter and the efficiencies, both for the signal and for the meter, are measured independently. The detuning and the signal phase ϕ_s are free fitting parameters.

In addition to the curves already compared with the experimental results, we show in Figure 11 the contributions of the different noise sources to the power spectrum $S_{X_s X_s}$ plotted in Fig. 4. The contribution of the cavity phase noise cancels at the bare oscillator frequency, as

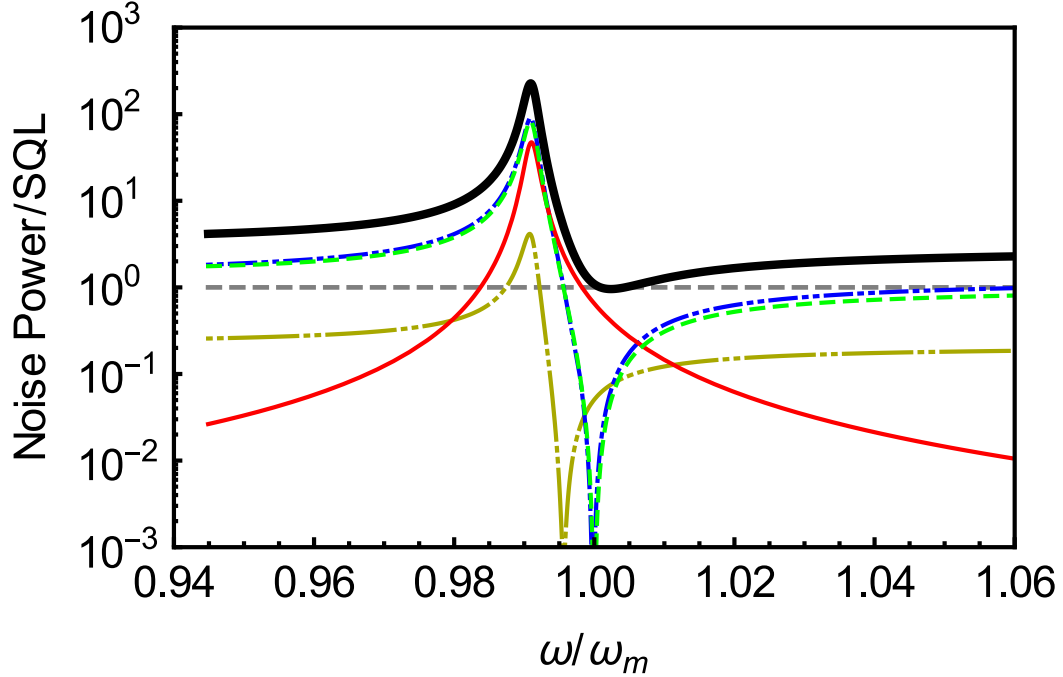


FIG. 11: Theoretical calculation of the spectrum reported in Figure 4 (black solid line), normalized to SQL (grey dashed line), together with its contributions: input laser noise (blue dashed-double dotted line), thermal noise (red solid line), vacuum noise entering through cavity losses (dark yellow, long dash-double dotted line), cavity phase noise (green dashed line).

discussed in Ref. [21]. The contribution of the laser noise (quantum noise and classical amplitude noise) reaches a minimum at a frequency determined by the best destructive interference between the fluctuations of the laser field (modified by the optical cavity) and those mediated by

the optomechanical interaction (originated by the term proportional to δq in Eq. (23)). With the parameters used for this spectrum, even this interference occurs close to ω_m . This coincidence allows to observe ponderomotive squeezing, that would otherwise be hidden by the cavity phase noise. The squeezing depth is actually limited by thermal noise.

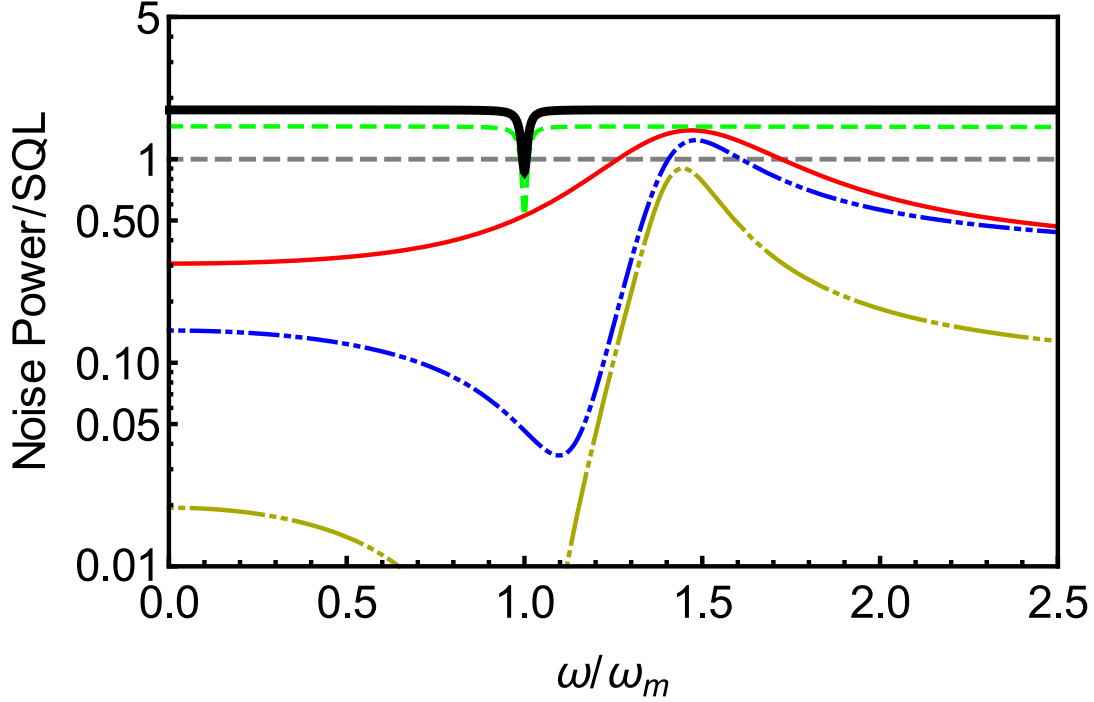


FIG. 12: Theoretical calculation of the spectrum of the residual fluctuations of X_s , reported in Figure 4 (black solid line), normalized to SQL (grey dashed line). The other curves show the contributions of the different noise sources to the final spectrum. We start by a system with just the laser noise, at zero temperature, without cavity losses and without extra displacement noise (dark yellow, long dash-double dotted line). We then add cavity losses (blue dashed-double dotted line), thermal noise (red solid line), cavity phase noise (green dashed line). The inclusion of vacuum noise introduced by the detection efficiency brings to the final spectrum.

In Figure 12 we show, for the same parameters, the spectrum of the residual fluctuations of X_s after the subtraction of the correlation with the meter. To put into evidence the different noise

contributions, we start by the residual spectrum where just the laser noise is present, than we add cavity losses, thermal noise and cavity phase noise. Here the interference described before is no more necessary to fall below the SQL, and the region where it happens is potentially much larger. However, in agreement with the comment to the previous figure, we see that the cavity phase noise strongly limits the width of this QND region. Its cancellation at ω_m is crucial, while the minimum of the spectrum is again limited by thermal noise.

* Electronic mail: marin@fi.infn.it

- [1] Braginsky, V. B., Vorontsov, Y. I., Thorne, K. S. Quantum nondemolition measurements. *Science* 209, 547-557 (1980).
- [2] Caves, C. M., Thorne, K. S., Drever, R. W. P., Sandberg, V. D., Zimmermann, M. On the measurement of a weak classical force coupled to a quantum-mechanical oscillator. I. Issues of principle. *Rev. Mod. Phys.* 52, 341-392 (1980).
- [3] Braginsky, V. B., Khalili, F. Y. Quantum nondemolition measurements: the route from toys to tools. *Rev. Mod. Phys.* 68, 1-11 (1996).
- [4] Grangier, P., Levenson, J. A. and Poizat, J.-P. Quantum non-demolition measurements in optics. *Nature (London)* 396, 537-542 (1998).
- [5] Jacobs, K., Tombesi, P., Collett, M. J., Walls, D. F. Quantum-nondemolition measurement of photon number using radiation pressure. *Phys. Rev. A* 49, 1961-1966 (1994).
- [6] Heidmann, A., Hadjar, Y., Pinard, M. Quantum nondemolition measurement by optomechanical coupling. *Appl. Phys. B* 64, 173-180 (1997).
- [7] Verlot, P., Tavernarakis, A., Briant, T., Cohadon, P.-F., Heidmann, A. Scheme to probe optomechanical correlations between two optical beams down to the quantum level. *Phys. Rev. Lett.* 102, 103601 (2009).
- [8] Verlot, P., Tavernarakis, A., Molinelli, C., Kuhn, A., Antoni, T., Gras, S., Briant, T., Cohadon, P.-F., Heidmann, A., Pinard, L., Michel, C., Flaminio, R., Bahriz, M., Le Traon, O., Abram, I.,

- Beveratos, A., Braive, R., Sagnes, I., Robert-Philip, I. Towards the experimental demonstration of quantum radiation pressure noise. *C. R. Physique* 12, 826-836 (2011).
- [9] Holland, M. J., Collett, M. J., Walls, D. F., Levenson, M. D. Nonideal quantum nondemolition measurements. *Phys. Rev. A* 42, 2995-3005 (1990).
- [10] Aspelmeyer, M., Kippenberg, T. J., Marquardt, F. Cavity optomechanics. *Rev. Mod. Phys.* 86, 1391-1452 (2014).
- [11] Murch, K. W., Moore, K. L., S. Gupta, Stamper-Kurn, D. M. Observation of quantum-measurement backaction with ultracold atomic gas. *Nat. Phys.* 4, 561-564 (2008).
- [12] Purdy, T. P., Peterson, R. W., Regal, C. A. Observation of radiation pressure shot noise on a macroscopic object. *Science* 339, 801-804 (2013).
- [13] Matsumoto, N., Komori, K., Michimura, Y., Hayase, G., Aso, Y., Tsubono, K. 5-mg suspended mirror driven by measurement-induced backaction. *Phys. Rev. A* 92, 033825 (2015).
- [14] Purdy, T. P., Grutter, K. E., Srinivasan, K., Taylor, J. M. Observation of optomechanical quantum correlations at room temperature. *arXiv:1605.05664* (2016).
- [15] Brooks, D. W. C., Botter, T., Schreppler, S., Purdy, T. P., Brahms, N., Stamper-Kurn, D. M. Non-classical light generation by quantum-noise-driven cavity optomechanics. *Nature (London)* 488, 476-480 (2012).
- [16] Safavi-Naeni, A. H., Grblacher, S., Hill, J. T., Chan, J., Aspelmeyer, M., Painter, O. Squeezed light from a silicon micromechanical resonator. *Nature (London)* 500, 185-189 (2013).
- [17] Purdy, T. P., Yu, P.-L., Peterson, R. W., Kampel, N. S., Regal, C. A. Strong optomechanical squeezing of light. *Phys. Rev. X* 3, 031012 (2013).
- [18] Serra, E., Borrielli, A., Cataliotti, F. S., Marin, F., Marino, F., Pontin, A., Prodi, G. A., Bonaldi, M. A low-deformation mirror micro-oscillator with ultra-low optical and mechanical losses. *Appl. Phys. Lett.* 101, 071101 (2012)
- [19] Borrielli, A., Pontin, A., Cataliotti, F. S., Marconi, L., Marin, F., Marino, F., Pandreaud, G., Prodi, G. A., Serra, E., Bonaldi, M. Low-loss optomechanical oscillator for quantum-optics experiments. *Phys. Rev. Applied* 3, 054009 (2015).
- [20] Marino, F., Cataliotti, F. S., Farsi, A., Siciliani de Cumis, M., Marin, F. Classical signature of

- ponderomotive squeezing in a suspended mirror resonator. *Phys. Rev. Lett.* 104, 073601 (2010).
- [21] Pontin, A., Biancofiore, C., Serra, E., Borrielli, A., Cataliotti, F. S., Marino, F., Prodi, G. A., Bonaldi, M., Marin, F., Vitali, D. Frequency-noise cancellation in optomechanical systems for ponderomotive squeezing. *Phys. Rev. A* 89, 033810 (2014).
- [22] Mancini, S. and Tombesi, P. Quantum noise reduction by radiation pressure. *Phys. Rev. A* 49, 4055-4065 (1994).
- [23] Fabre, C., Pinard, M., Bourzeix, S., Heidmann, A., Giacobino, E. and Reynaud, S. Quantum-noise reduction using a cavity with a movable mirror. *Phys. Rev. A* 49, 1337-1343 (1994).
- [24] Kimble, H. J., Levin, Y., Matsko, A. B., Thorne, K. S. and Vyatchanin, S. P. Conversion of conventional gravitational-wave interferometers into quantum nondemolition interferometers by modifying their input and/or output optics. *Phys. Rev. D* 65, 022002 (2001).
- [25] Serra, E., Bonaldi, M., Borrielli, A., Marin, Marconi, L., Marino, F., Pandraud, G., Pontin, A., Prodi, G. A., Sarro, P. M. Fabrication and characterization of low loss MOMS resonators for cavity opto-mechanics. *Microelectron. Eng.* 145, 138-142 (2015).
- [26] Cohadon, P. F., Heidmann, A., Pinard, M. Cooling of a mirror by radiation pressure. *Phys. Rev. Lett.* 83, 3174-3177 (1999).
- [27] Pontin, A., Bonaldi, M., Borrielli, A., Marino, F., Marconi, L., Bagolini, A., Pandraud, G., Serra, E., Prodi, G. A., Marin, F. Dynamical back-action effect in low loss optomechanical oscillators. *Ann. Phys. (Berlin)* 527, 89-99 (2015).